AGU PUBLICATIONS

Water Resources Research

TECHNICAL REPORTS: METHODS

10.1002/2017WR021913

On the Texture Angle Detection Used in Space-Time Image Velocimetry (STIV)

Ryota Tsubaki[1]

[1]Department of Civil Engineering, Nagoya University, Nagoya, Japan

Abstract The space-time image velocimetry (STIV) method evaluates the velocity of a water surface by analyzing a texture angle within a space-time image (STI) obtained from an image sequence of the flowing water's surface. The brightness gradient tensor (BGT) has been utilized for calculating the texture angle of the STI within the original STIV. The BGT is sensitive to image quality, especially high-frequency noise, and this fact limits the capability and accuracy of the velocity estimation. The objectives of this study were to understand why the BGT is sensitive to high-frequency noise and how to resolve this defect. In the manuscript, derivation of the BGT is first reviewed and then a geometric representation of the BGT is discussed. The reason the BGT is sensitive to high-frequency noise is also discussed, and, then, based on geometric representations of the BGT, a measure to improve this defect is proposed. To demonstrate differences between the two methods, texture angles from artificial and field image sets were also analyzed using the BGT and the improved BGT.

Key Points:
- Convective water surface flow can be estimated from a texture angle in a space-time image made from a flowing water video
- Space-time image velocimetry (STIV) utilizes the brightness gradient tensor (BGT) for estimating the texture angle to evaluate water surface flow
- This study clarifies why the BGT is sensitive to high-frequency noise and suggests a more robust algorithm for estimating the texture angle

Correspondence to:
R. Tsubaki,
rtsubaki@civil.nagoya-u.ac.jp

Citation:
Tsubaki, R. (2017). On the texture angle detection used in space-time image velocimetry (STIV). *Water Resources Research*, *53*, 10,908–10,914. https://doi.org/10.1002/2017WR021913

Received 21 SEP 2017
Accepted 15 NOV 2017
Accepted article online 21 NOV 2017
Published online 21 DEC 2017

1. Introduction

1.1. Need for an Accurate and Robust Velocimeter for Free Surface Flow in the Field

Accurate measurement of the flow velocity of the free surface in rivers, lakes, and oceans is absolutely essential for understanding the processes occurring in such environments. Accurate estimations of flow are also indispensable for managing water resources and for preventing the damage caused by water flow. Both accuracy and the capability for robust and continuous estimations of flow are required for such practical applications. As a method for quantifying flow, imaging techniques have several advantages. Particle image velocimetry (PIV) is one of the most widely used methods for quantifying flow. The application of PIV as a tool in velocimetry began as flume experiments accompanied by controlled laser lighting and particle seeding. The use of PIV to free surfaces in the field has also been applied (Fujita et al., 1998; Holland et al., 2001; Jodeau et al., 2008; Le Coz et al., 2010) and has contributed to better understanding for the processes occurring in flooding rivers (e.g., Gunawan et al., 2012; Tsubaki et al., 2011) and coastal regions (e.g., Holland et al., 2001). Application of the PIV to riverine surfaces is sometimes referred to as large-scale PIV (LSPIV) and has been reviewed, for example, in Muste et al. (2008) and Kantoush et al. (2011). The primary instrument required for conducting PIV in the field is a video camera. Since video cameras (wide varieties in price, size, and performance) are available for purchase in the marketplace and since most mobile phones have built-in video cameras, video cameras are widespread. Existing survey cameras are easily utilized for flow quantification (e.g., Tsubaki et al., 2011) and flood observations via public involvement can readily be implemented (e.g., Le Boursicaud et al., 2016).

1.2. One-Component Image Velocimetry Using a Space-Time Image

PIV and LSPIV are widely used methods for measuring two-component velocity in a two-dimensional distribution. Other than PIV/LSPIV, an imaging technique utilizing a space-time image (STI) made from a continuous image sequence also exists (Chickadel et al., 2003; Fujita & Tsubaki, 2002; see Figure 1). The texture angle, θ, within the STI, is directly related to the convection velocity, U, of image pattern motion, as well as to the space coordinate of the STI (Figure 1d). This relationship can be described as follows:

$$U = dx/dt = 1/\tan\theta. \tag{1}$$

The relationship indicates that we can quantify the velocity component of image motion, U, by evaluating the texture angle, θ, within a STI. An algorithm is necessary for quantifying the texture angle. Figure 2 provides examples of a raw STI made from image sequences of river flow. As indicated in the figure, STIs generally consist of a mixture of patterns that have different space-time scales. Accordingly, a robust algorithm for accurate and stable

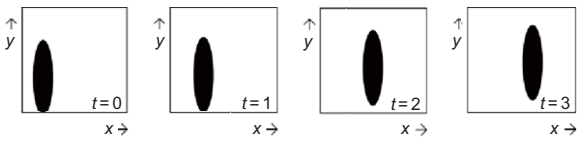

(a) Time-series 2D images.

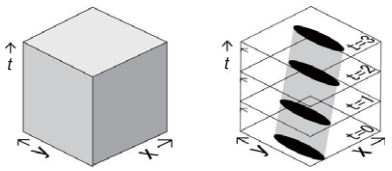

(b) A time-stacked image (3D).

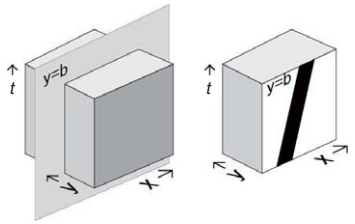

(c) A 2D space-time image obtained by time-slicing the 3D time-stacked image.

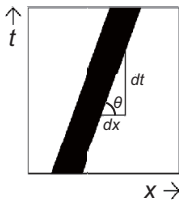

(d) The texture-angle in the space-time image.

Figure 1. The relationship between time series images, the space-time image, and the texture angle in the space-time image.

texture angle detection from a complicated pattern is critical when applying the STIV for quantifying flow in fields without dispersing seeding particles. The time and spatial scales of the STI have been determined based on the surface pattern scale. In fields, the conditions of the surface pattern, the lighting, and the weather are changed and cannot be controlled. These factors change the characteristics and quality of STIs.

Fujita and Tsubaki (2002) estimated the texture angle by maximizing a pattern similarity function for a deformed STI with different angles. Chickadel et al. (2003) applied a two-dimensional Fourier transform to the STI and a coordinate transformation was applied to the Fourier transformed STI in order to obtain a velocity-streamwise wave number image. Chickadel et al. (2003) named their method the optical current meter (OCM) and applied it for analyzing nearshore surface currents. Puleo et al. (2012) applied the OCM in order to detect the cross-sectional velocity distribution in a river. Fujita et al. (2007) utilized the brightness gradient tensor (BGT) for calculating the pattern gradient (detail is described in section 1.3). Fujita et al. (2007) compared STIV and LSPIV in lab and field images and discussed the applicability of the two methods. Yu et al. (2015) proposed a method for detecting the angle by searching the peak of an auto-correlation coefficient of the STI. To be more specific, they divided the STI into odd and even rows and reconstructed two images composed of odd and even rows for the original STI. They, then, calculated the cross correlation between odd and even row images along the space-coordinate. The space-coordinate lag provided a maximum correlation corresponding to *dx* in Figure 1d. One of the motivations of Yu et al. (2015) for developing a new method was to overcome the limited capability of the BGT algorithm in detecting the representative texture angle from a complicated pattern.

1.3. The Brightness Gradient Tensor (BGT) Method

Here I review the BGT approach used in Fujita et al. (2007). For the approach, the inner product of a unit vector having an arbitrary direction, $\boldsymbol{n}$, and a local gradient of brightness, $\nabla i_{x,t}$, takes its maximum when the directions of $\boldsymbol{n}$ and $\nabla i_{x,t}$ are identical. $\nabla i_{x,t}^T \boldsymbol{n}$ takes a value of zero when $\boldsymbol{n}$ and $\nabla i_{x,t}$ are orthogonal. To estimate the representative angle of pattern θ for a specific domain, A, $\nabla i_{x,t}^T \boldsymbol{n}$ can be assumed as an error indicator and finding the representative pattern angle for domain A can be replaced with a problem of finding $\boldsymbol{n}$, which provides the least square of $\nabla i_{x,t}^T \boldsymbol{n}$ integrated for the domain A (Jahne, 1993):

$$\min_{\boldsymbol{n}} \int_A \left(\nabla {i_{x,t}}^T \boldsymbol{n}\right)^2 dxdt. \tag{2}$$

The least square approach was used for achieving uniqueness of the solution and equally evaluating the bidirectional gradient of brightness (this matter will be discussed in section 2.1). The obtained $\boldsymbol{n}$ from equation (2) is parallel to the pattern direction (and perpendicular to $\nabla i_{x,t}$) so the problem is identical to one that finds the angle of $\boldsymbol{n}$, providing the maxima of this integral, if $\boldsymbol{n}$ is defined as the direction perpendicular to the pattern. Thus:

$$\max_{\boldsymbol{n}} \int_A \left(\nabla {i_{x,t}}^T \boldsymbol{n}\right)^2 dxdt. \tag{3}$$

The equation can be rearranged to:

$$\max_{\boldsymbol{n}} \boldsymbol{n}^T \left(\int_A \nabla i_{x,t} \nabla {i_{x,t}}^T dxdt \right) \boldsymbol{n}, \tag{4}$$

and the integral in equation (4), corresponding to the area integrated brightness gradient tensor, BGT, becomes:

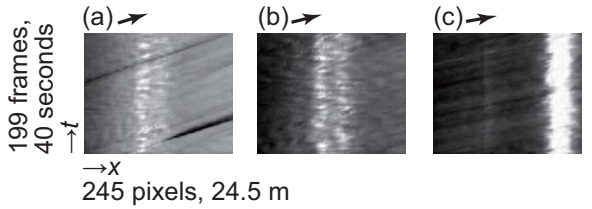

Figure 2. Examples of space-time images obtained from a video sequence of flow in the Tempaku River, Japan. The gray-scale range was adjusted to highlight the patterns. The vector above each swatch depicts the representative texture angle detected by the eye.

$$\boldsymbol{J}=\int_A \nabla i_{x,t}\,\nabla i_{x,t}{}^T\,dxdt. \tag{5}$$

The maximizing equation (4) can be substituted by rotating the BGT into the principal axes coordinate as:

$$\begin{bmatrix}\lambda_1 & 0\\ 0 & \lambda_2\end{bmatrix}=\begin{bmatrix}\cos\varphi & \sin\varphi\\ -\sin\varphi & \cos\varphi\end{bmatrix}\boldsymbol{J}\begin{bmatrix}\cos\varphi & -\sin\varphi\\ \sin\varphi & \cos\varphi\end{bmatrix}, \tag{6}$$

where λ_1 and λ_2 are the eigenvalues of the BGT (Jahne, 1993). Note that φ is an orthogonal to the pattern but that θ is defined parallel to the pattern (Figure 2). The off-diagonal components of equation (6) are:

$$\begin{aligned}0&=-\cos\varphi\sin\varphi\boldsymbol{J}_{11}+(\cos\varphi\cos\varphi-\sin\varphi\sin\varphi)\boldsymbol{J}_{12}+\cos\varphi\sin\varphi\boldsymbol{J}_{22}\\&=-\frac{1}{2}\sin 2\varphi\boldsymbol{J}_{11}+\cos 2\varphi\boldsymbol{J}_{12}+\frac{1}{2}\sin 2\varphi\boldsymbol{J}_{22},\end{aligned} \tag{7}$$

then, equation (7) can be summarized as:

$$\frac{2\boldsymbol{J}_{12}}{\boldsymbol{J}_{11}-\boldsymbol{J}_{22}}=\frac{\sin 2\varphi}{\cos 2\varphi}=\tan 2\varphi. \tag{8}$$

Here the components of the BGT are:

$$\begin{aligned}\boldsymbol{J}_{11}&=\int_A \frac{\partial i_{x,t}}{\partial x}\frac{\partial i_{x,t}}{\partial x}dxdt,\\ \boldsymbol{J}_{12}&=\int_A \frac{\partial i_{x,t}}{\partial x}\frac{\partial i_{x,t}}{\partial t}dxdt, \text{ and}\\ \boldsymbol{J}_{22}&=\int_A \frac{\partial i_{x,t}}{\partial t}\frac{\partial i_{x,t}}{\partial t}dxdt.\end{aligned} \tag{9}$$

The BGT method is quite sensitive to small patterns included within the STI (Fujita et al., 2007; Yu et al., 2015). To overcome this limitation, the following two techniques have been employed: (1) applying smoothing filters including the fast Fourier transformation (FFT) low-pass filter (Hara & Fujita, 2010) onto the STI, and (2) decomposing the STI domain into smaller portions and calculating a representative angle by weighted averaging proportional to pattern clarity in each decomposed subarea. Clarity of the pattern is evaluated using a scalar known as coherency (Fujita et al., 2007; Jahne, 1993) and value ranges from 0 to 1.

1.4. The Objective of This Study

The objective of this study was to improve the excessive sensitivity of the BGT to small patterns. To achieve this objective, in sections 2.1 and 2.2, using a geometric interpretation of the BGT, I discuss the reason the BGT method is quite sensitive to small patterns. A well-balanced method for estimating the texture angle is proposed in section 2.3. As proof of concept, in section 3, image angles with various patterns are evaluated using the original BGT and the well-balanced method. Research findings obtained in this study are summarized in section 4.

2. The Pattern Gradient Estimation

In this section, the BGT, originally obtained based on a tensor calculation, is geometrically interpreted. The reason the BGT is quite sensitive to small patterns is then discussed based on a geometrical interpretation of the BGT. Finally, a countermeasure for overcoming extreme sensitivity to small patterns is presented.

2.1. Geometric Interpretation of the BGT

For a case of $\boldsymbol{n}$ and $\nabla i_{x,t}$ directed in the opposite direction, the inner product, $\nabla i_{x,t}^T\,\boldsymbol{n}$, becomes negative. As shown in Figure 3, a stripe pattern within the STI provides the bidirectional components of the brightness gradient, $\nabla i_{x,t}$. To estimate the primal direction of the pattern, the square of $\nabla i_{x,t}^T\,\boldsymbol{n}$ is a better indicator because the bidirectional components can be identically evaluated.

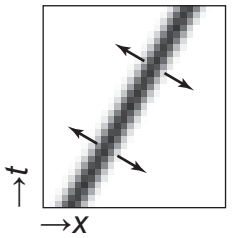

Figure 3. An example of the bidirectional components of the brightness gradient, $\nabla i_{x,t}$, made from the one stripe pattern.

The local gradient of brightness, $\nabla i_{x,t}$, can be represented by the unit vector, $\boldsymbol{n_i}$, and the slope, s, as follows:

$$\nabla i_{x,t} = \begin{bmatrix} \frac{\partial i_{x,t}}{\partial x} \\ \frac{\partial i_{x,t}}{\partial t} \end{bmatrix} = s\boldsymbol{n}_i, \tag{10}$$

thus:

$$\begin{aligned} \frac{\partial i_{x,t}}{\partial x} &= s\boldsymbol{n}_{i,x} = s\ \cos\alpha, \text{ and} \\ \frac{\partial i_{x,t}}{\partial t} &= s\boldsymbol{n}_{i,t} = s\ \sin\alpha, \end{aligned} \tag{11}$$

here α is the angle of the local gradient. By substituting equation (11) into equation (8), we obtain:

$$\begin{aligned} \tan 2\varphi &= \frac{2\boldsymbol{J}_{12}}{\boldsymbol{J}_{11}-\boldsymbol{J}_{22}} = \frac{2\int_A \frac{\partial i_{x,t}}{\partial x}\frac{\partial i_{x,t}}{\partial t}dxdt}{\int_A \frac{\partial i_{x,t}}{\partial x}\frac{\partial i_{x,t}}{\partial x}dxdt - \int_A \frac{\partial i_{x,t}}{\partial t}\frac{\partial i_{x,t}}{\partial t}dxdt} \\ &= \frac{2\int_A s^2\cos\alpha\ \sin\alpha\, dxdt}{\int_A s^2\cos\alpha\ \cos\alpha\, dxdt - \int_A s^2\sin\alpha\ \sin\alpha\, dxdt} \\ &= \frac{\int_A s^2\sin 2\alpha\, dxdt}{\int_A s^2\frac{\cos 2\alpha+1}{2}dxdt - \int_A s^2\frac{1-\cos 2\alpha}{2}dxdt} = \frac{\int_A s^2\sin 2\alpha\, dxdt}{\int_A s^2\cos 2\alpha\, dxdt}. \end{aligned} \tag{12}$$

The last expression can be geometrically interpreted by integrating the vector components originating from the brightness gradient (Figure 4a). However, the angle is doubled (Figure 4b). By assuming that the local slope of the gradient, s, is constant, a pair of counter directional gradients (e.g., $\alpha = 0$ and π) become parallel ($\alpha' = 0$ and 2π) and a pair of orthogonal direction gradients (e.g., $\alpha = 0$ and 0.5π) become counter directional ($\alpha' = 0$ and π) within the double-angled field (Figure 4b), respectively. Therefore, the original counter directional components are amplified and the orthogonal components cancel one another within the integral in equation (12).

2.2. On the Response of the BGT to High-Frequency Noise

For simplicity, in section 2.1, the local slope, s, in equation (12) is assumed to be constant although this is not true for most situations. Figure 4c provides an example of the pattern obtained using a different gradient slope. The left-hand side of the stripe has a steeper slope but a smaller area, and the right-hand side has a milder and wider area. In the integral in equation (12), the squared slope, s^2, is accounted for and the texture angle estimation using the BGT method is highly weighted to the texture angle within the area containing a steeply sloped gradient. As shown in Figure 4c, the result causes no problems for simple patterns. The pattern shown in Figure 4d is also simple, but problematic for the BGT due to the steep slope of the gradient at the top and bottom of the box. The BGT method may detect the aligned angle at the top and bottom of the box, not the angle of the vertical sides that appear dominant to the eye because the majority of the area composes the vertical gradation stripe. The BGT method is sensitive to a steep sloped gradient with a limited area and tends to discount smoothed patterns with a large spatial (and temporal) scale. The BGT approach has been used with smoothing image filters, including the low-pass FFT filter, because the BGT is too sensitive to steep slope gradients. Using smoothing filters, these steep slope gradients can be

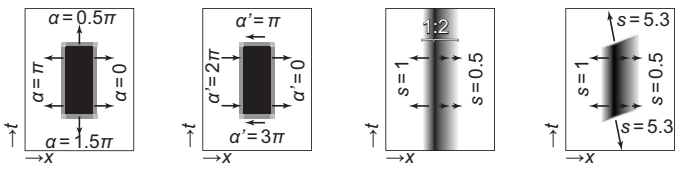

Figure 4. A schema of the brightness gradient distributions. The vectors schematically show gradients at each point. The parameters α and s are the angle and slope of the brightness gradient, respectively. (a) The distribution of the original gradient. (b) The vector field of the double-angled gradient, α'. (c) The vector field of the asymmetric stripe pattern. (d) The vector field of the asymmetric box pattern.

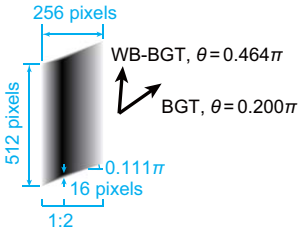

Figure 5. Representative angles calculated using the WB-BGT and BGT for the asymmetric box pattern (Figure 4d). Note that the angle here is θ and is defined parallel to the pattern. Neither the angle was orthogonal to the pattern, φ, nor to the local gradient angle, α.

removed prior to BGT calculation. Domain decomposition of the STI into small portions also works well for detecting smooth patterns with a large area because the majority of the decomposed subarea can be expected to contain a smooth pattern in many, if not all, situations.

2.3. The Well-Balanced Method

The original BGT is sensitive to a steep slope because of s^2 in equation (12). The squares originate from equation (3). To equally evaluate a pair of opposite directing brightness gradients, a squared $(\nabla i_{x,t}^T \boldsymbol{n})$ is used in equation (3). As illustrated in Figures 4a and 4b, this objective is realized using the double-angled trigonometric functions in equation (12). To avoid problems arising from the square of s, the local brightness gradient vector, equation (10), is rearranged to:

$$\nabla i_{x,t} = \sqrt{s}\boldsymbol{n}_i, \tag{13}$$

and by repeating formula manipulations between equations (3) and (9), we obtain:

$$\tan 2\varphi = \frac{\int_A \sqrt{s}\sin 2\alpha \, dxdt}{\int_A \sqrt{s}\cos 2\alpha \, dxdt}. \tag{14}$$

instead of equation (12). Equation (14) contains no square of s and can detect the direction of the longer axis of the box shown in Figure 4d because the steeply sloped top and bottom sides (shown as vectors with $s = 5.3$ in Figure 4d) have a limited area as compared to the vertical sides. Thus, the gradient on the top and bottom sides is almost neglected, but the gradient on the vertical sides is weighted in the integrals shown in equation (14). This texture angle detection method is essentially identical to the method described in Hiraku and Suzuki (1990) and was utilized in order to detect the velocity distribution from sequential images obtained using high-speed cameras (Hiraku & Suzuki, 2000). Hereafter, I refer to this model as the well-balanced BGT (WB-BGT).

3. Proof of Concept

3.1. Artificial Images

To demonstrate the difference in angle estimations using the BGT and WB-BGT, I analyzed the asymmetric box pattern provided in Figure 4d. The results are shown in Figure 5. As seen in Figure 5, both the BGT and WB-BGT angles were affected by the vertical left- and right-hand sides and aligned top and bottom. The WB-BGT angle was biased to the vertical pattern ($\theta = 0.5\pi$). On the other hand, the BGT angle was highly impacted by the angle of the top and bottom sides ($\theta = 0.111\pi$).

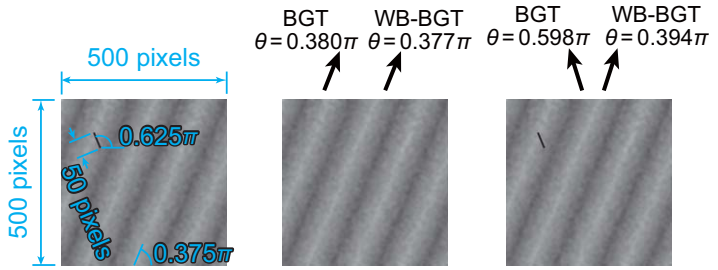

(a) Dimensions of the artificial image with scratch noise.

(b) Detected angles from the artificial image without scratch noise.

(c) Detected angles from the artificial image with scratch noise.

Figure 6. Artificial images with and without a small scratching noise of 5 pixels in width and 50 pixels in length. (a) The dimensions of the image without noise. (b) Angles detected by the BGT and the WB-BGT for an image without noise. (c) Angles detected by the two methods for an image with noise.

Figure 6 provides examples of the difference in the angle estimation using more realistic images. Here a wave pattern having a 0.375π decline angle was combined with a Gaussian noise pattern. Then, short, thin, but dense, lines with a 0.625π angle of 5 pixels in width and 50 pixels long were overlain to mimic a scratching noise having a high-frequency component (Figure 6a). Such high-frequency noises are caused by the intersection of birds/insects, raindrops the on camera cover (column noise), or light and lightning reflection to the space-time slice (row noise). Figure 6b displays angles detected by the BGT and the WB-BGT for an image without noise. Both methods provide a reasonable estimation of the angle for an image without noise. For an image with noise, as shown in Figure 6c, the BGT provides an angle corresponding to the angle of the noise pattern, whereas the WB-BGT successfully estimated the angle of the background wave pattern. As discussed in sections 2.2 and 2.3, the difference was caused by the nature of the BGT and the WB-BGT methods.

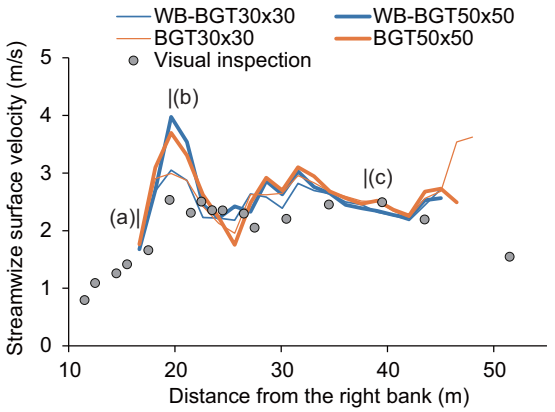

Figure 7. The cross-sectional velocity distribution analyzed from field images. The thin lines are the result of using a 30 by 30 pixel window for the local gradient calculation, whereas the thick lines display a 50 by 50 pixel window result. Labels (a), (b), and (c) in the plot correspond to the cross section of the STIs (a), (b), and (c) shown in Figure 2.

3.2. Field Images

STI images from a field were analyzed. STIs were made from a video obtained using a CCTV camera installed at the Nonami Bridge station of the Tempaku River, Japan, from 1:10 A.M. to 1:35 A.M. for the August 29, 2008 flood event (for details, see Tsubaki et al., 2011). As benchmark velocity data, the trajectories for 17 clearly visible pieces of floating debris and a float were manually inspected and the streamwise velocity components at various cross-sectional locations were evaluated. The texture angles for 24 STIs made at different cross-sectional locations were analyzed using the BGT and the WB-BGT and are compared in Figure 7. Prior to obtaining a representative angle for each STI, the local gradient and the coherency distribution were calculated and a smaller window size (30 by 30 pixels) and a larger window size (50 by 50 pixels) were used (Fujita et al., 2007). With the exception of the outlier found for BGT within the 30 by 30 pixel window, smaller window size cases (the two thin lines in Figure 7) displayed better agreement for the visual inspection result. The WB-BGT with 30 by 30 pixel windows displayed better agreement as compared to the others. The root-mean-square error between the visual inspection and the STIV results were 0.34, 0.39, 0.46, and 0.49 m/s for WB-BGT30x30, BGT30x30, WB-BGT50x50, and BGT50x50, respectively.

3.3. Discussion

The BGT is quite sensitive to high-frequency patterns so, paradoxically, the angle of the subarea (window) containing high-frequency noise can, statistically, be easily removed. However, the WB-BGT provides an intermediate value between the mixture of patterns and it is difficult to distinguish the value affected by noise. For cases when the noise is quite episodic, a BGT with statistical outlier rejection may provide better performance. If the high-frequency noise is widely distributed (e.g. noise due to discretization error during image compression), the WB-BGT may provide a robust result, as suggested in Figure 7. A well-balanced approach is needed for quantitatively comparing the amplitude of wave patterns for different wave lengths.

4. Conclusions

In this study, derivation of the BGT was reviewed and then a geometric representation of the BGT was discussed. Based on this representation, the reason the BGT is quite sensitive to high-frequency noise was interpreted. This shortcoming of the BGT can be managed using small equation modifications. The derived WB-BGT was identical to the method described in Hiraku and Suzuki (1990). This study also revealed the linkage between the BGT and Hiraku and Suzuki (1990). To illustrate differences between the two methods, texture angles for the two image sets were analyzed using the BGT and the WB-BGT. If the texture consists of low- and high-frequency patterns, the BGT tends to only detect a high-frequency pattern angle but the WB-BGT can detect an angle of texture having larger amplitude and a wider coverage area. Due to this, the WB-BGT is more robust for the noisy image sets frequently obtained in the field under adverse conditions such as rain, wind, and nighttime recording. Thus, this study contributes to the goal of achieving a robust and continuous estimation procedure for obtaining the surface velocity of free surface flow from images and better supports our understanding of the processes occurring in water flows in the field and the management of water resources. Two case studies are not enough to generalize conclusions for field measurements under various conditions. The optimal combination of image preprocessing methods and angle detection methods must be further investigated to assess and improve robustness for real-world measurements.

Notation

$i_{x,t}$ the brightness of space-time image (STI) at (x, t).
$\boldsymbol{J}_{xt}$ the brightness gradient tensor (BGT).
$\boldsymbol{n}$ the unit vector of the representative orthogonal (except for $\boldsymbol{n}$ used in equation (2)) angle of texture for the STI.

$\boldsymbol{n}_i$ the unit vector of the local brightness gradient vector.
s the slope of the local brightness gradient vector.
U the velocity component of image flow along the x coordinate of the STI.
x, t the coordinates of space and time in the STI, respectively.
α the angle of the local brightness gradient.
θ the representative texture angle of the STI.
φ the representative orthogonal angle of texture within the STI.

Acknowledgments
This study was supported by: (1) a research and development grant for river and sediment control by the Ministry of Land, Infrastructure, Transport and Tourism (MLIT), Japan, and (2) JSPS KAKENHI grant JP16K06609, JP17K06574, and JP17K06575. The data used in this study are available from the corresponding author.

References

Chickadel, C. C., Holman, R. A., & Freilich, M. H. (2003). An optical technique for the measurement of longshore currents. *Journal of Geophysical Research*, *108*(C11), 3364. https://doi.org/10.1029/2003JC001774

Fujita, I., Muste, M., & Kruger, A. (1998). Large-scale particle image velocimetry for flow analysis in hydraulic engineering applications. *Journal of Hydraulic Research*, *36*(3), 397–414.

Fujita, I., & Tsubaki, R. (2002). *A novel free-surface velocity measurement method using spatio-temporal images*. Paper presented at Hydraulic measurements and experimental methods 2002, American Society of Civil Engineers, Estes Park, CO.

Fujita, I., Watanabe, H., & Tsubaki, R. (2007). Development of a non-intrusive and efficient flow monitoring technique: The space-time image velocimetry (STIV). *International Journal of River Basin Management*, *5*(2), 105–114.

Gunawan, B., Sun, X., Sterling, M., Shiono, K., Tsubaki, R., Rameshwaran, P., . . . Fujita, I. (2012). The application of LS-PIV to a small irregular river for inbank and overbank flows. *Flow Measurement and Instrumentation*, *24*, 1–12.

Hara, H., & Fujita, I. (2010). Application of two dimensional fast Fourier transform to river surface flow measurement with space time image (in Japanese). *Annual Journal of Hydraulic Engineering, JSCE*, *54*, 1105–1110.

Hiraku, R., & Suzuki, T. (1990). A technique to measure the flow velocity by an analysis of tracer pathline images (2nd report) (in Japanese). *Journal of the Kansai Society of Naval Architects, Japan*, *214*, 56–64.

Hiraku, R., & Suzuki, T. (2000). Development of particle image velocimetry (PIV) by processing sequential image data with high-speed video camera (in Japanese). *Transactions of the Japan Society of Mechanical Engineers Series B*, *66*(642), 346–351. https://doi.org/10.1299/kikaib.66.346

Holland, K. T., Puleo, J. A., & Kooney, T. N. (2001). Quantification of swash flows using video-based particle image velocimetry. *Coastal Engineering*, *44*(2), 65–77.

Jahne, B. (1993). *Spatio-temporal image processing* (pp. 143–152). New York: Springer-Verlag.

Jodeau, M., Hauet, A., Paquier, A., Le Coz, J., & Dramais, G. (2008). Application and evaluation of LS-PIV technique for the monitoring of river surface velocities in high flow conditions. *Flow Measurement and Instrumentation*, *19*(2), 117–127.

Kantoush, S. A., Schleiss, A. J., Sumi, T., & Murasaki, M. (2011). LSPIV implementation for environmental flow in various laboratory and field cases. *Journal of Hydro-Environment Research*, *5*(4), 263–276.

Le Boursicaud, R., Pénard, L., Hauet, A., Thollet, F., & Le Coz, J. (2016). Gauging extreme floods on YouTube: Application of LSPIV to home movies for the post-event determination of stream discharges. *Hydrological Processes*, *30*(1), 90–105.

Le Coz, J., Hauet, A., Pierrefeu, G., Dramais, G., & Camenen, B. (2010). Performance of image-based velocimetry (LSPIV) applied to flash-flood discharge measurements in Mediterranean rivers. *Journal of Hydrology*, *394*(1), 42–52.

Muste, M., Fujita, I., & Hauet, A. (2008). Large-scale particle image velocimetry for measurements in riverine environments. *Water Resources Research*, *44*, W00D19. https://doi.org/10.1029/2008WR006950

Puleo, J. A., McKenna, T. E., Holland, K. T., & Calantoni, J. (2012). Quantifying riverine surface currents from time sequences of thermal infrared imagery. *Water Resources Research*, *48*, W01527. https://doi.org/10.1029/2011WR010770

Tsubaki, R., Fujita, I., & Tsutsumi, S. (2011). Measurement of the flood discharge of a small-sized river using an existing digital video recording system. *Journal of Hydro-Environment Research*, *5*(4), 313–321.

Yu, K., Kim, S., & Kim, D. (2015). Correlation analysis of spatio-temporal images for estimating two-dimensional flow velocity field in a rotating flow condition. *Journal of Hydrology*, *529*, 1810–1822.